λ-MnO_2 Thin Films with Sponge-Like Structures: Synthesis, Characterization and Physiochemical Applications

Khalid Abdelazez Mohamed Ahmed[1,2*]

[1]*Department of Chemistry, Faculty of Science and Technology, Al-Neelain University, P.O. Box 12702, Khartoum, Sudan*

[2]*Department of Chemistry, University College - Khurma, Taif University, P.O. Box 11099, Taif 21944, Saudi Arabia*

* ***Corresponding author:***

tel: +966-552639984
email: khalidgnad@hotmail.com

Received: February 28, 2021
Accepted: June 12, 2021

DOI: 10.22146/ijc.64392

Abstract: *Manganese dioxide has acquired significant research attentiveness in many fields over the past years because of its exciting physicochemical features. The magnetized λ-MnO_2 thin films with sponge-like structures (TSLs) were prepared by hydrothermal-soft chemical and delithiation-lithium manganese process. The XRD, XPS, EDX, FESEM, TEM, HR-TEM, and N_2 adsorption-desorption techniques were used to characterize the as-prepared product's structure composition, morphology, and surface area. The particle growth details of λ-MnO_2 are postulated by the oxidation-ionic change-delithiation (OID) mechanism. The electrochemical property was analyzed by galvanostatic discharge-charging, electrochemical impedance spectrum (EIS), and cyclic voltammetry (CV). Special attention of λ-MnO_2 S.L.s is given to their applications in the degradation of methyl orange (MO) from wastewater under O_2 air bubble pump and cathodic substance in the lithium-ion battery. Due to the peculiarity crystal form and morphology face, the λ-MnO_2 TSLs might be promisingly applied in the various physicochemical area.*

Keywords: *manganese dioxide; sponge-like; cathode; methyl orange*

■ INTRODUCTION

Azo dyes such as methyl orange (MO) are textile dye used in food, paper, and leather industries. However, the release of MO and their products from the environment causes severe pollution problems [1]. Metal-oxide such as ZnO, TiO_2, ZrO_2, and WO_3, with different morphologies, have recently been utilized as catalysts to degrade various dangerous pollutants [2-5]. Mn-based oxides are extensively applied as a cathode material in battery technologies due to their outstanding structural flexibility, low cost, abundance, toxicity, and environmental friendliness [6-10]. Among the various manganese(IV) oxide forms, λ-MnO_2 has been used widely as a material for metal-air batteries [11], fuel cells [12], supercapacitors [13], anodic materials [14-15], and catalytic water oxidation [11,16]. The implementation of λ-MnO_2 as cathodic material in Zn-Mn redox flow batteries [17], Mg-ion batteries [18] was recently reported.

Recently, several authors have considered the properties of nanomaterials to depend not only on chemical compositions but also on their shape and size including their synthetic and the processes route [19-20]. In particular, MnO_2 nanostructures with different crystallographic forms originated in one-dimensional such as nanobelts [21], nanorods, nanowires [22], nanotubes [23-24], and nanofibers [25-26] morphologies have been achieved by several routes such as hydrothermal, sol-gel and electrospinning technique methods. In terms of λ-MnO_2, few reports are applied to fabricate the nanoparticles and nanodisks using microemulsion, macroporous cellulose gel beads, and delithiation-lithium manganese process in an acid medium [27-29]. Nevertheless, one of the challenges in materials science is to prepare nanostructure with desirable properties and structures form in proper ways. To the best of our information, this is the first time to synthesize lambda manganese dioxide with sponge-like structure (λ-MnO_2 TSLs).

In this paper, the λ-MnO_2 TSLs were obtained by the hydrothermal-soft chemical process of permanganate with lithium perchlorate in benzaldehyde

solution under acidic treatment. Due to its noteworthy physicochemical characteristics, λ-MnO_2 TSLs was used as cathodic materials for lithium-ion batteries and catalytic degradation of methyl orange through air bubble pumping in an aqueous solution.

■ EXPERIMENTAL SECTION

Materials

All analytical grade reactants and solvents, including $KMnO_4$, $LiClO_4$, benzaldehyde, ethylene carbonate, dimethyl carbonate, and methylene orange (MO), were used without any additional purification and purchased from Techno Pharma. Chem. Vardhman City Center Delhi, India, and New Jersey, USA.

Instrumentation

The crystal structures of the samples were measured by X-ray diffractometer (Panalytical X' Pert Pro; Netherlands) using a Cu Ka target (ʎ = 1.5418 Å) at an angular 2θ speed of 2°/min. Energy Dispersive X-ray Spectrometry (EDS) EDAX spectrometer was utilized with Agilent 6510 in positive ionization mode mass in ranges of 50–600 Da. The chemical elements in the composite powders were analyzed by X-ray photoelectric spectroscopy (XPS) employing Kratos Analytical Axis Ultra DLD with Al K_{a1} radiation. For the broad spectrum, the X-ray photon energy of 1.486 kV was used with a passage of 160 eV in the range 0–1200 eV. FEI Sirion, 200, Netherlands (FE-SEM) model microscope was used to outlook morphologies. Tecnai $G^2$20, Netherlands, (TEM) images were used to investigate the morphologies parameters and SA-ED. The lattice distance and growth direction were examined by high-resolution transmission electron microscopy (HR-TEM) image and was performed on a JEM-2010 FEF TEM at an acceleration voltage of 200 kV. The magnetic properties (M-H curve) were measured at 5 K on an ADE 4HF vibrating sample magnetometer.

Procedure

Synthesis of λ-MnO_2 thin films

In a typical procedure, 0.5 mmol (79 mg) of $KMnO_4$, 0.012 mmol (1.28 mg) of $LiClO_4$, and 0.4 mL of benzaldehyde were mixed and added into a 50 mL Teflon-lined stainless steel autoclave, sealed and heated at 120 °C for 10 h in an electric oven. The autoclave was cooled to room temperature (25 °C). The product was collected by centrifugation at 8,000 rpm for 5 min and washed with distilled water and absolute ethanol several times, followed by drying in an oven at 50 °C for 12 h. The autoclave results were pre-treated in 0.5 M aqueous sulfuric acid solution under magnetic stirring for 1 h.

Electrochemical test

Electrochemical descriptions were achieved by utilizing the lithium foils in both counter and reference electrodes. About 85% of the mentioned sample was adequately mixed with 5% polytetrafluoroethylene (PTFE) in absolute ethanol. The slurry materials were pressed uniformly onto black thin film by twining roller and dried in an electric vacuum oven at 60 °C for 24 h. The electrodes were modified to a chip in a diameter of 12 mm with the mass weight of 1.0–1.2 mg/cm^2. Ultimately, electrode films were replaced into an Ar-replete glove box and ingathered with M $LiClO_4$ in ethylene carbonate:dimethyl carbonate (1:1 v/v) as the electrolyte solution under room temperature. The cell battery was tested in the voltage of 0.01–4.00 V versus Li^+/Li. Cyclic voltammetry (CV) curves were examined on a CHI600E electrochemical workstation under a scanner rate of 0.5 mV/s and a potential of 0.01 to 4.00 V. Electrochemical impedance spectroscopy (EIS) was carried out in the range from 0.01 Hz to 100 kHz.

Catalytic test

The catalytic degradation of the MO process was conducted in a three-neck glass under a reflux condenser, magnetic stirring, and oxygen air bubble at room temperature. A suspension of 0.5 mmol (0.043 g) catalyst powder was added in 200 mL of aqueous MO (0.1 g/L) solution. At regular intervals, the samples were taken from the reactor container after removing the powder by filtration and centrifugation. Varian Cary 50 Bio UV/Visible Spectrophotometer was used to analyze the disintegration of dye. The degradation efficiency % was calculated by this equation: (Degradation efficiency = $(A_o-A_t)/A_o \times 100$), where A_o is the absorption in the beginning of reaction and A_t is the absorption after a specific time of reaction.

■ RESULTS AND DISCUSSION

Fig. 1(a) describes the X-ray diffraction patterns of the as-synthesized sample. The diffraction patterns peaks show a highly crystalline of λ-MnO_2 with a cubic phase structure and a lattice parameter of 0.803 nm in the space group of Fd-3m (no. 227). The XRD diffraction pattern corresponds to the standard data of JCPDS card no. 44-0992 (Fig. 1(b)). No other peaks were detected for impurity stages and un-reacted precursors.

In other ways, the choice of substance and element composition was identified by EDX analysis (Fig. 1(c)). The element affirmation of the product affirms the apparition of Mn and O elements with atomic weight of 1:2 and the chemical structure of MnO_2. XPS is a beneficial technique to reveal the surface chemistry and chemical bonding in the resultant particles. Fig. 2(a) offered that XPS Mn 2*p* region and an asymmetrical main of Mn $2p_{3/2}$ peak in the presence of Mn^{3+} and Mn^{4+} (Fig. 2(b)), which in the present a multiplet splitting of the λ-MnO_2 spectrum with satellite peaks at 655 and 641 eV and it referred to MnO_6 octahedral body which is similar to the earlier studies [15,30].

Different magnification images investigated the morphology and size of the as-prepared sample. As shown in Fig. 3(a), the low-SEM photograph reveals that the precursor presents in wire structure. Accuracy analysis by high-magnification SEM, thin-film wire exposed consists of ultra-long nanowires with average thickness size of 10–20 nm and length longer than 6 mm (Fig. 3(b)). To further verify the sample, TEM analysis is utilized to check the nanosize dimension of λ-MnO_2 (Fig. 3(c)). The corpus of the nanowires is like FE-SEM observation. The selected area electron diffraction (SA-ED) pattern (insert in Fig. 3(c)) indicating the λ-MnO_2 TSLs has a single crystal structure. As depicted in Fig. 3(d), the formation of single-crystalline 1D-TSLs is evidenced by well-aligned lattice lines in the HR-TEM images. The interplanar distance calculated from the lattice fringe of 0.202 nm denotes to {400} plane of λ-MnO_2.

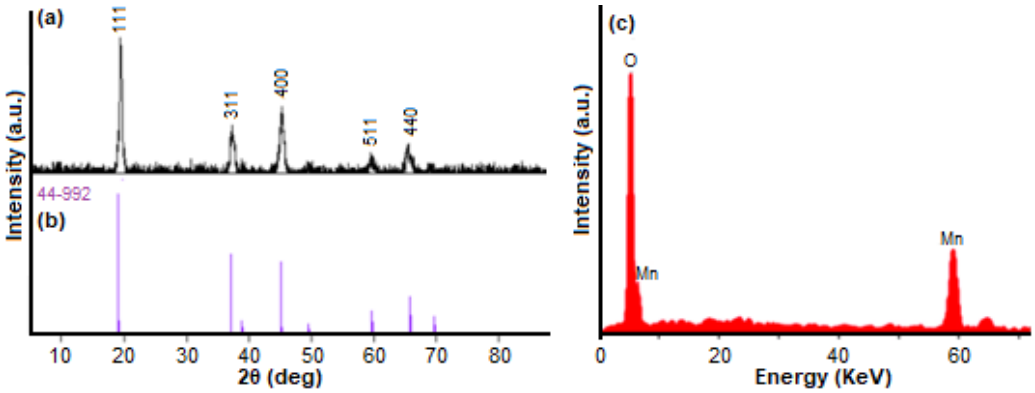

Fig 1. (a) XRD pattern, (b) JCPDS card file, and (c) EDS spectra of λ-MnO_2 TSLs

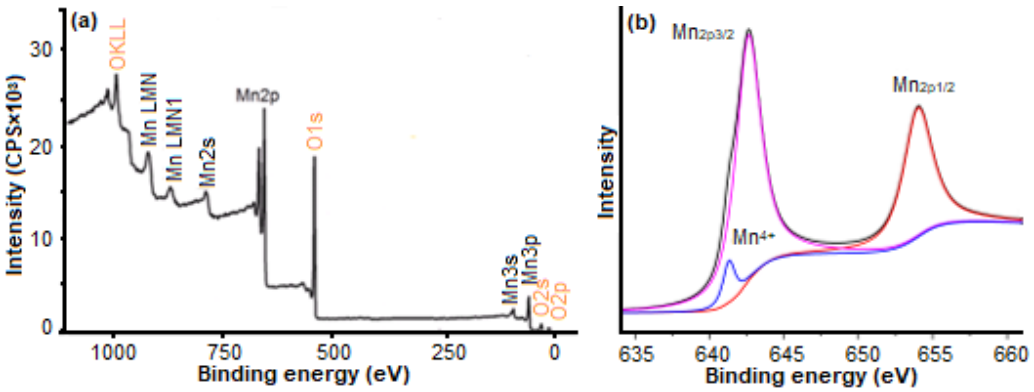

Fig 2. (a) XPS analysis and (b) photoelectron spectra of Mn 2*p* in λ-MnO_2 TSLs

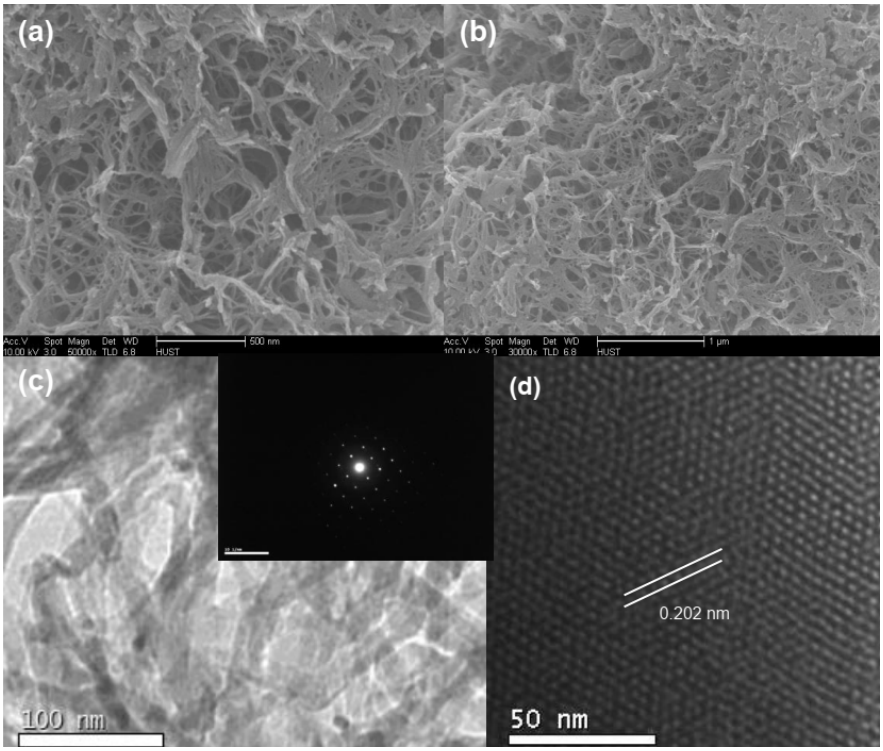

Fig 3. (a) Low-magnification SEM images, (b) High-magnification SEM images; (c) TEM image (SA-ED pattern) and (d) HR-TEM images of λ-MnO_2 TSLs

The BET surface area of λ-MnO_2 TSLs analysis was examined by nitrogen adsorption-desorption isotherm. Fig. 4(a) depicts that the S_{BET} of λ-MnO_2 TSLs is 19 m^2/g, which the isotherm curve is typically a slightly mesoporous substance with a type IV of Brunauer-Deming-Deming-Teller (BDDT) loops [31]. As debated, the mixture of Mn^{3+} and Mn^{4+} valence state in λ-MnO_2 alludes to one of the reasons for the ferromagnetic organizing-spinal behavior at low temperatures. The M-H curves evidence in (Fig. 4(b)), reveals the super-paramagnetic property of λ-MnO_2 TSLs in saturation magnetic moment either per mass unit at 5 K. Due to current results and recent reports [11,16], the formation of MnO_2 crystal with the occupation of Mn and O ions in the octahedral 16d sites and 32e sites, is constructed by treating lithium manganese oxides in dilute acid solution.

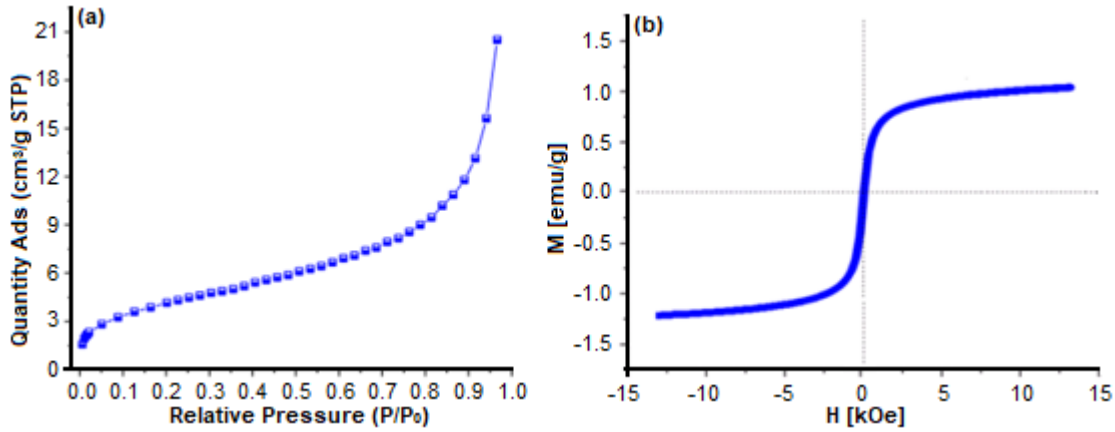

Fig 4. (a) N_2 adsorption-desorption isotherm curve, and (b) M-H curve of λ-MnO_2 TSLs

The mechanism of growth TSLs particles is likely considered for the amalgamation process following the previous reports [16,21]. Fig. 5 clarifys the following steps of crystal growth through schematically anisotropic structures. The formation of λ-MnO_2 TSLs in our current work is closely related to the benzaldehyde and hydrothermal-soft chemical process condition. $KMnO_4$ may oxidize the benzaldehyde to benzoic acid and become reduced to birnessite. Furthermore, lithium manganese oxide may be produced under the ionic exchange process by the lithiation of birnessite in the oven. λ-MnO_2 TSLs are formed via delithiation of lithium manganese oxides in an acidic medium during the OID process.

The electrochemical property of λ-MnO_2 TSLs is investigated with different techniques. Fig. 6(a) shows that CV curves are exhibited in the first cathodic scan cycle, with two reduction peaks at 0.3 and 0. 65 V that is evidence for coinciding with the electrolyte apportionment and following the construction of solid electrolyte interphase (SEI) layer generation. In the anodic orientation, one peak of oxidation at 1.3 V signalize that attributable to the delithiation process from the lithiated manganese oxide matrices and the dissociation of Li_2O [30-31].

However, the galvanostatic charge-discharge electrode displaying a reversible capacity of λ-MnO_2 TSLs is about 180 mAh g^{-1} (Fig. 6(b)). After 50 cycles (Fig. 6(c)), the capacitor residue is 156 mAh g^{-1}. This result suggests that the lithium-ion capacitor may be affected by phase morphology and spinal structures of MnO_2. As shown in Fig. 6(d), the significantly lower charge-transfer resistance in a smaller semicircle at the high-frequency region of MnO_2 TSLs (65 Ω) promotes improved electron delivery and Li-ion diffusion to increased specific capacitance. It is useful for application as cathode material in the lithium-ion battery.

The catalytic behavior of λ-MnO_2 TSLs in MO dye degradation is studied. Fig. 7(a) shows the UV-vis absorption spectrum of MO solution before and after degradation catalyzed by λ-MnO_2 TSLs under air bubbles at various time intervals. It can be seen from the spectra, before the treatment, the UV-vis spectrum of MO consists of two prominent characteristic absorption bands. One peak in the visible region (464 nm) has referred to as an

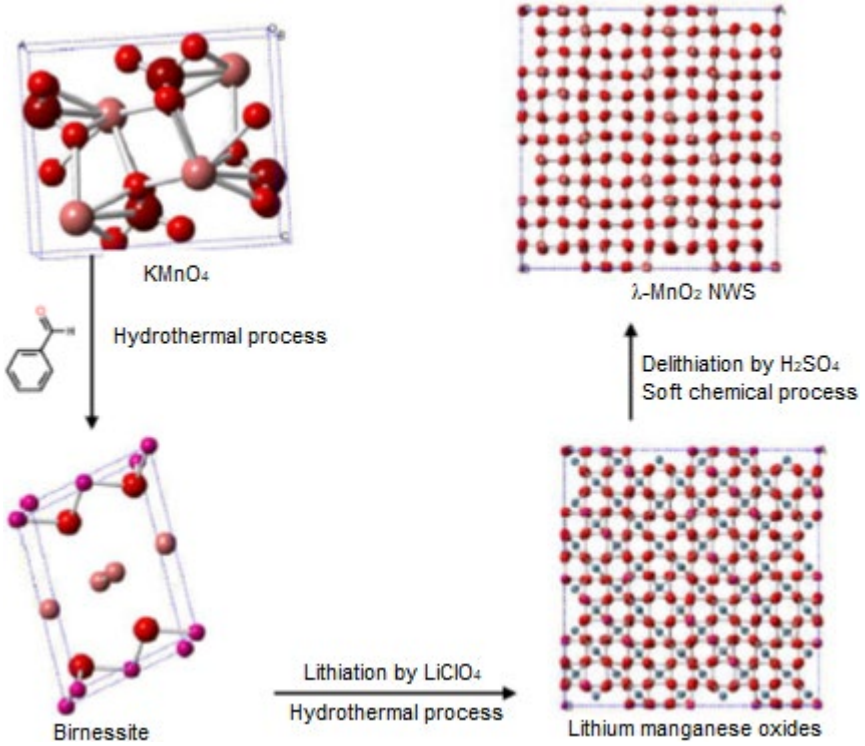

Fig 5. Schematic elucidation of reaction process included in the synthesis of λ-MnO_2 TSLs

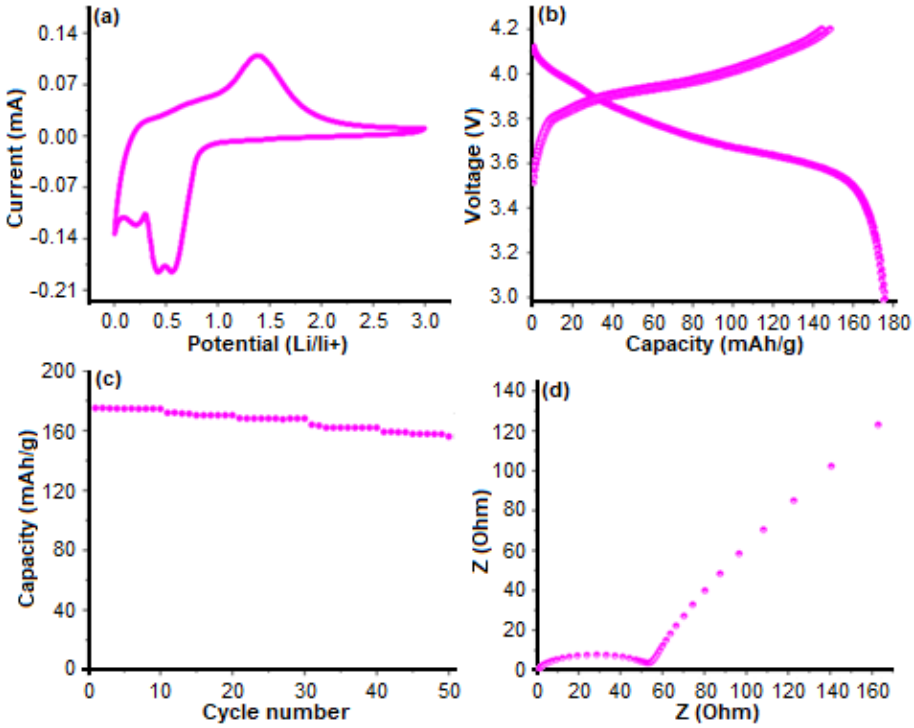

Fig 6. (a) Cyclic voltammograms, (b) galvanostatic charge-discharge profile, (c) Nyquist plots, and (d) rate capacity fading of λ-MnO_2 TSLs

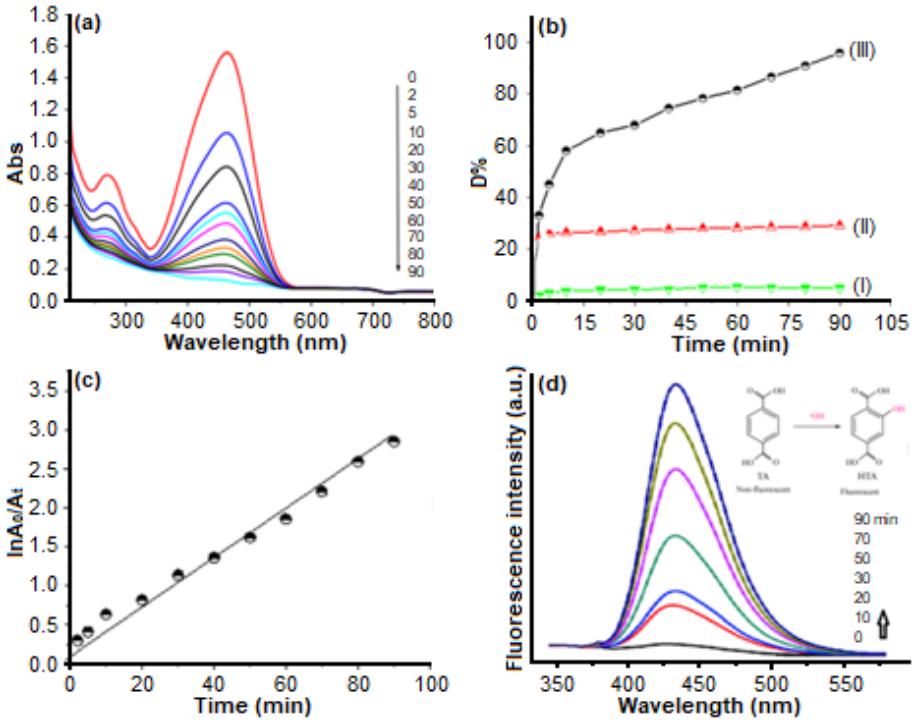

Fig 7. (a) UV-vis spectra of degradation products of MO with air bubble pumping catalyzed by λ-MnO_2 TSLs in aqueous solutions for different times, (b) the degradation percentages of MO followed by air bubble pumping (I); by λ-MnO_2 TSLs (II); λ-MnO_2 TSLs-air bubble pumping (III) and (d) Photoluminescence spectra change of terephthalic acid in various time

azo bond, and the other peak in the U.V. region (272 nm) is associated with an aromatic ring [32]. When λ-MnO_2 TSLs treated MO solution in the presence of O_2 air bubbles, the absorption intensity of peaks is decreased with time; it suggested that MO is gradually degraded of the aromatic ring. Several impulse tests were carried out to study the influencing factors of MO dye degradation, such as the catalyst powder and O_2-air pumping. As shown in Fig. 7(b), the degradation percentage (D%) of MO followed by without catalyst (I), absent oxygen (II), and with catalyst under O_2 air pumping (III). Curves (I) and (II) display that the MO hardly degraded when performed under O_2-air or catalyst only, respectively. The rapid degradation of MO with an average of 96% efficiency is achieved by λ-MnO_2 TSLs under O_2-air following. This result suggests that air bubbles are necessary, but the oxygen flow rate has no significant effect on the degradation process.

Due to the surplus of oxygen bubbles, the chemical kinetics of degradation of MO on λ-MnO_2 TSLs catalyst is considered pseudo-1st-order reactions. As shown in Fig. 7(c), the plots of $\ln(A_o/A_t)$ vs. times per minute are straight lines. The rate constant may be calculated using $[K = \ln(A_o/A_t)/t]$. From the plots, the rate constants for the degradation of MO catalyzed by λ-MnO_2 TSLs is 0.0143 min^{-1}. Based on previous results [33-34], the possible mechanism for removing MO on λ-MnO_2 TSLs catalyst is supported under O_2-air bubble and room light conditions as the following equations.

$$\lambda - MnO_2 + h\nu \rightarrow e^- + h^+ \quad (1)$$

$$e^- + O_2 \rightarrow O_2\bullet^- \quad (2)$$

$$H_2O + h^+ \rightarrow OH\bullet + H^+ \quad (3)$$

$$O_2^- + H^+ \rightarrow \bullet HO_2 \quad (4)$$

$$\bullet OH + MO \rightarrow \text{degradation products} \quad (5)$$

Previously several authors have investigated the degradation of methyl orange by manganese oxide, which is required to anesthetize the elements or intermediate reaction under a Fenton-like process [35-36]. At present, λ-MnO_2 TSLs may effectively motivate O_2 and H_2O molecules into hydroxyl radicals under the room light irradiation, confirmed by terephthalic acid photoluminescence the radical probing techniques in solution with irradiation times (Fig. 7(d)). The piecemeal rise of emission intensity at 430 nm band is due to the reaction of intermediate hydroxyl radicals with terephthalic acid. The above results indicate that the insertion may permeate a particular physical property without regard to the importance of the listed element but rather the medical role and function.

■ CONCLUSION

In conclusion, the λ-MnO_2 TSLs with magnetic, electrochemical, and catalytic efficiencies are synthesized via the hydrothermal-soft chemical process. The suitable formation mechanism of λ-MnO_2 TSLs is suggested by the OID process. The hysteresis loop of λ-MnO_2 TSLs belays a strong magnetic contrast. The electrochemical properties of the product provide faster Li^+ and electron kinetics and effectively alleviate the volume change during catholic lithium insertion-extraction. It exhibits novel constructors as well as outstanding rate capability and sterling cycling ability of capacity ~180 mAh g^{-1} retained after 50 cycles. The catalytic test revealed good catalytic degradation of MO under oxygen air bubble pumping, which is attributed to high crystallinity, unique magnetic, and one dimension particles. Therefore, our findings open up unexplored possibilities for these materials, leading to the expansion of various physiochemical applications.

■ ACKNOWLEDGMENTS

The author kindly thanks the financial support from the Vice Presidency of Graduate Studied and Academic Research, Taif University- Saudi Arabia.

■ REFERENCES

[1] Shan, R., Lu, L., Gu, J., Zhang, Y., Yuan, H., Chen, Y., and Luo, B., 2020, Photocatalytic degradation of methyl orange by Ag/TiO_2/biochar composite catalysts in aqueous solutions, *Mater. Sci. Semicond. Process.*,114, 105088.

[2] Khan, R., Hassan, M.S., Cho, H.S., Polyakov, A.Y., Khil, M.S., and Lee, I.H., 2014, Facile low-temperature synthesis of ZnO nanopyramid and its application to photocatalytic degradation of methyl

orange dye under UV irradiation, *Mater. Lett.*, 133, 224–227.

[3] Shen, Y., Wang, W., and Xiao, K., 2016, Synthesis of three-dimensional carbon felt supported TiO_2 monoliths for photocatalytic degradation of methyl orange, *J. Environ. Chem. Eng.*, 4 (1), 1259–1266.

[4] Basahel, S.N., Ali, T.T., Mokhtar, M., and Narasimharao, K., 2015, Influence of crystal structure of nanosized ZrO_2 on photocatalytic degradation of methyl orange, *Nanoscale Res. Lett.*, 10 (1), 73.

[5] Zheng, Q., and Lee, C., 2014, Visible light photoelectrocatalytic degradation of methyl orange using anodized nanoporous WO_3, *Electrochim. Acta*, 115, 140–145.

[6] Zhang, K., Kim, D., Hu, Z., Park, M., Noh, G., Yang, Y., Zhang, J., Lau, V.W., Chou, S.L., Cho, M., Choi, S.Y., and Kang, Y.M., 2019, Manganese based layered oxides with modulated electronic and thermodynamic properties for sodium ion batteries, *Nat. Commun.*, 19, 5203–5215.

[7] Misnon, I.I., Aziz, R.A., Zain, N.K.M., Vidhyadharan, B., Krishnan, S.G., and Jose, R., 2014, High performance MnO_2 nanoflower electrode and the relationship between solvated ion size and specific capacitance in highly conductive electrolytes, *Mater. Res. Bull.*, 57. 221–230.

[8] Lao-atiman, W., Julaphatachote, T., Boonmongkolras, P., and Kheawhom, S., 2017, Printed transparent thin film Zn-Mn_{O2} battery, *J. Electrochem. Soc.*, 164 (4), A859.

[9] Suren, S., and Kheawhomm, S., 2016, Development of a high energy density flexible zinc-air battery, *J. Electrochem. Soc.*, 163 (6), A846.

[10] Khamsanga, S., Pornprasertsuk, R., Yonezawa, T., Mohamad, A.A., and Kheawhom, S., 2019, δ-MnO_2 nanoflower/graphite cathode for rechargeable aqueous zinc ion batteries, *Sci. Rep.*, 9 (1), 8441.

[11] Lee., S., Nam, G., Sun, J., Lee, J.S., Lee, H.W., Chen, W., Cho, J., and Cui, Y., 2016, Enhanced intrinsic catalytic activity of λ-MnO_2 by electrochemical tuning and oxygen vacancy generation, *Angew. Chem. Int. Ed.*, 55 (30), 8459–8765.

[12] Musil, M., Choi, B., and Tsutsumi, A., 2016, λ-MnO_2 positive electrode for fuel cell/battery systems, *J. Electrochem. Soc.*, 163, A2047.

[13] Xue, Y., Chen, Y., Zhang, M.L., and Yan, Y.D., 2008, A new asymmetric supercapacitor based on λ-MnO_2 and activated carbon electrodes, *Mater. Lett.*, 62, 3884–3886.

[14] Li, L., Qu, W., Liu, F., Zhao, T., Zhang, X., Chen, R., and Wu, F., 2014, Surface modification of spinel λ-MnO_2 and its lithium adsorption properties from spent lithium ion batteries, *Appl. Surf. Sci.*, 315, 59–65.

[15] Yuan, C., Zhang, Y., Pan, Y., Liu, X., Wang, G., and Cao, D., 2014, Investigation of the intercalation of polyvalent cations (Mg^{2+}, Zn^{2+}) into λ-MnO_2 for rechargeable aqueous battery, *Electrochim. Acta*, 116, 404–412.

[16] Robinson, D.M., Go, Y.B., Greenblatt, M., and Dismukes, G.C., 2010, Water oxidation by λ-MnO_2: Catalysis by the cubical Mn_4O_4 subcluster obtained by delithiation of spinel $LiMn_2O_4$, *J. Am. Chem. Soc.*, 132 (33), 11467–11469.

[17] Liu, N., Mohanapriya, K., Pan, J., Hu, Y., Sun, Y., and Liu, X., 2020, A facile preparation of λ-MnO_2 as cathode material for high-performance zinc-manganese redox flow battery, *J. Electrochem. Soc.*, 167 (4), 040517.

[18] Chen, W., Zhan, X., Luo, B., Ou, Z., Shih, P.C., Yao, L., Pidaparthy, S., Patra, A., An, H., Braun, P.V., Stephens, R.M., Yang, H., Zuo, J.M., and Chen, Q., 2019, Effects of particle size on Mg^{2+} ion intercalation into λ-MnO_2 cathode materials, *Nano Lett.*, 19 (7), 4712–4720.

[19] Khan, I., Saeed, K., and Khan, I., 2019, Nanoparticles: Properties, applications and toxicities, *Arabian J. Chem.*, 12 (7), 908–931.

[20] Ahmed, K.A.M., Zeng, Q., Wu, K., and Huang, K., 2010, Mn_3O_4 nanoplates and nanoparticles: Synthesis, characterization, electrochemical and catalytic properties, *J. Solid State Chem.*, 183 (3), 744–751.

[21] Ahmed, K.A.M., Abbood, H.A., and Huang, K., 2012, Hydrothermal synthesis of Mn(OH)O nanowires and their thermal conversion to (1D)-

manganese oxides nanostructures, *J. Cryst. Growth*, 358, 33–37.

[22] Tang, W., Shan, X., Li, S., Liu, H., Wu, X., and Chen, Y., 2014, Sol-gel process for the synthesis of ultrafine MnO_2 nanowires and nanorods, *Mater. Lett.*, 132, 317–321.

[23] Shen, M., Wang, Y., and Zhang, Y.X., 2020, Neatly arranged mesoporous MnO_2 nanotubes with oxygen vacancies for electrochemical energy storage, *Dalton Trans.*, 49 (48), 17552–17558.

[24] Zheng, D., Sun, S., Fan, W., Yu, H., Fan, C., Cao, G., Yin, Z., and Song, X., 2005, One-step preparation of single crystalline β-MnO_2 nanotubes, *J. Phys. Chem. B*, 109 (34), 16439–16443.

[25] Xu, K., Li, S., Yang, J., and Hu, J., 2018, Hierarchical hollow MnO_2 nanofibers with enhanced supercapacitor performance, *J. Colloid Interface Sci.*, 513, 448–454.

[26] Zhao, L., Yu, J., Li, W., Wang, S., Dai, C., Wu, J., Bai, X., and Zhi, C., 2014, Honeycomb porous MnO_2 nanofibers assembled from radially grown nanosheets for aqueous supercapacitors with high working voltage and energy density, *Nano Energy*, 4, 39–48.

[27] Greedan, J.E., Raju, N.P., Wills, A.S., Morin, C., Shaw, S.M., and Reimers, J.N., 1998, Structure and magnetism in λ-MnO_2 geometric frustration in a defect spinel, *Chem. Mater.*, 10 (10), 3058–3067.

[28] Wang, N., Cao, X., Lin, G., and Shih, Y., 2007, λ-MnO_2 nanodisks and their magnetic properties, *Nanotechnology*, 18, 475605–475608.

[29] Kim, S., Lee, J., Kang, J.S., Jo, K., Kim, S., Sung, Y.E., and Yoon, J., 2015, Lithium recovery from brine using a λ-MnO_2/activated carbon hybrid supercapacitor system, *Chemosphere*, 125, 50–56.

[30] Kim, S., Kang, J.S., Joo, H., Sung, Y.E., and Yoon, J., 2020, Understanding the behaviors of λ-MnO_2 in electrochemical lithium recovery: Key limiting factors and a route to the enhanced performance, *Environ. Sci. Technol.*, 54 (14), 9044–9051.

[31] Yuan, Y., and Cheng, L., 2012, Theoretical prediction for the structures of gas phase lithium oxide clusters: $(Li_2O)_n$ (n = 1–8), *Int. J. Quantum Chem.*, 113 (9), 1264–1271.

[32] Nasrollahzadeh, M.S., Hadavifar, M., Ghasemi, S.S., and Chamjangali, M.A., 2018, Synthesis of ZnO nanostructure using activated carbon for photocatalytic degradation of methyl orange from aqueous solutions, *Appl. Water Sci.*, 8 (4), 104.

[33] Xia, H., Xiao, W., Lai, M.O., and Lu, L., 2009, Facile synthesis of novel nanostructured MnO_2 thin films and their application in supercapacitors, *Nanoscale Res. Lett.*, 4 (9), 1035.

[34] Ahmed, K.A.M., Peng, H., Wu, K., and Huang, K., 2011, Hydrothermal preparation of nanostructured manganese oxides (MnO_x) and their electrochemical and photocatalytic properties, *Chem. Eng. J.*, 172 (1), 531–539.

[35] Yao, Y., Cai, Y., Wu, G., Wei, F., Li, X., Chen, H., and Wang, S., 2015, Sulfate radicals induced from peroxymonosulfate by cobalt manganese oxides ($Co_xMn_{3-x}O_4$) for Fenton-like reaction in water, *J. Hazard. Mater.*, 296, 128–137.

[36] Luo, S., Duan, L., Sun, B., Wei, M., Li, X., and Xu, A., 2015, Manganese oxide octahedral molecular sieve (OMS-2) as an effective catalyst for degradation of organic dyes in aqueous solutions in the presence of peroxymonosulfate, *Appl. Catal., B*, 164, 92–99.